



# HHS Public Access

Author manuscript

*J Magn Reson.* Author manuscript; available in PMC 2019 April 01.

Published in final edited form as:

*J Magn Reson.* 2018 April ; 289: 113–121. doi:10.1016/j.jmr.2018.02.013.

## Dielectric Properties of 3D-Printed Materials for Anatomy Specific 3D-Printed MRI coils

Bahareh Behzadnezhad<sup>1,2</sup>, Bruce D Collick<sup>1</sup>, Nader Behdad<sup>2</sup>, and Alan B McMillan<sup>1</sup>

<sup>1</sup>Department of Electrical and Computer Engineering, University of Wisconsin, Madison, WI 53706, USA

<sup>2</sup>Department of Radiology, Wisconsin Institute for Medical Research, University of Wisconsin, Madison, WI 53705, USA

### Abstract

Additive manufacturing provides a low-cost and rapid means to translate 3D designs into the construction of a prototype. For MRI, this type of manufacturing can be used to construct various components including the structure of RF coils. In this paper, we characterize the material properties (dielectric constant and loss tangent) of several common 3D-printed polymers in the MRI frequency range of 63 MHz to 300 MHz (for MRI magnetic field strengths of 1.5 T – 7 T), and utilize these material properties in full-wave electromagnetic simulations to design and construct a very low-cost subject/anatomy-specific 3D-printed receive-only RF coil that fits close to the body. We show that the anatomy-specific coil exhibits higher signal-to-noise ratio compared to a conventional flat surface coil.

### Keywords

3D printing; anatomy specific coils; radio-frequency (RF) coils; dielectric properties measurement; magnetic resonance imaging (MRI); electromagnetics; parallel RLC resonator

### Introduction

The recent availability of low-cost equipment for additive manufacturing (3D printing) has greatly reduced the burden of translating 3D designs into prototype construction. Additive manufacturing can be used in MRI to help build various components including phantom, holders, gradient coils, as well as the supporting structures of RF coils [1–3]. Traditionally, RF coils are constructed by hand or by printed circuit board (PCB) lithography techniques. These methods can be limited by labor-intensive manufacturing and two-dimensional fabrication methods. For the development of RF coils in MRI, additive manufacturing can provide a wider range of design freedom to build arbitrary geometry 3D coils that would be challenging to make with conventional approaches. Furthermore, current 3D-printers

**Publisher's Disclaimer:** This is a PDF file of an unedited manuscript that has been accepted for publication. As a service to our customers we are providing this early version of the manuscript. The manuscript will undergo copyediting, typesetting, and review of the resulting proof before it is published in its final citable form. Please note that during the production process errors may be discovered which could affect the content, and all legal disclaimers that apply to the journal pertain.

provide good structural precision with build resolution on the order of 10  $\mu\text{m}$  and enable rapid construction within timespan of several hours. In the future, state of the art conductor printing capability may eliminate the need to add conductive components (e.g. copper foil) and capacitors in MRI coils. [4,5]

The design of MRI coils with arbitrary 3D geometries requires extensive analytical expressions to analyze and calculate the inductance of the coil, where the use of EM simulations is an efficient and promising technique to expedite the design process [6–8]. In addition to the need for the knowledge of the electromagnetic field distribution inside the biological phantom, it is necessary to include the material properties (e.g., dielectric constant, loss tangent, thermal, and mechanical properties) of the coil components in the simulation. Dielectric constant or permittivity is the property that permits a medium to store energy in, and release energy from, an electric field. Dielectric loss or loss tangent determines the lossiness of a medium [9]. Including these material properties in electromagnetic simulations will result in optimized RF coil performance. Furthermore, accurate computer simulation enables fewer design iterations, allowing better estimation of discrete component values, and can reduce the time required to construct a coil.

The material used to construct the structural components of RF coils plays a crucial role in the frequency response and the achievable quality factor (Q), so knowledge of its electrical properties (especially dielectric constant and dielectric loss) is crucial. So far, Q factors have been evaluated for a 3D printed RF coil constructed with polylactic acid (PLA) [2] and some evaluation of dielectric properties of 3D printed material has been performed at microwave frequencies [10]. However, to the best of our knowledge, no parametric values of dielectric constant and dielectric loss for common 3D printing materials have been reported at MRI-relevant frequencies (e.g., 60–300 MHz).

The response of a non-magnetic material to RF waves depends primarily on the dielectric constant and loss tangent of the material. Therefore, precise characterization of permittivity and loss tangent of a material is necessary to enable robust design and simulation of RF and microwave circuits. To characterize these materials, many measurement techniques exist and can be classified as transmission line methods, free-space techniques, resonant methods, and open coaxial probes (near field sensors) [10,11]. However, all of the aforementioned approaches have limitations for characterizing materials for use in MRI RF coils.

In transmission line methods (microstrip-line and stripline methods) [12–14], a slab of the material under test is used as the insulating substrate of the transmission line or a waveguide is filled with the sample under test. In this method, the dielectric properties are extracted using information obtained from transmission and reflection coefficients of the wave from the sample filled region. The method is simple and thus relatively inexpensive, but sample preparation is challenging for lower frequencies due to the large wavelength of electromagnetic waves. For example, to consider a half-wavelength microstrip-line at 127.8 MHz, a sample of almost 1 m would be required.

An example of a free-space technique includes a system using two focusing lens antennas, one on each side of a planar sample to be characterized, connected to a vector network

analyzer (VNA) [15–17]. This method is suitable for relatively high microwave frequencies at which the physical sizes of the antennas and the focusing lenses are not excessively large. Application of this method to MRI relevant frequencies would require using very large antennas and focusing lenses as well as large sample sizes. This significantly increases the cost and complexity of such an approach for low RF and microwave frequencies (e.g. frequencies below 1 GHz).

In resonant cavity methods, the cavity is filled with the material under test (MUT) and the relevant properties are extracted based on a measured shift in resonance frequency and change in quality factor of the cavity [18]. Other than resonant cavity methods, microstrip-line resonator and circular resonator methods have also been used to characterize material properties. Although resonant techniques enable the most precise characterization methods, especially for low loss materials, they suffer from being applicable only at microwave frequencies (high MHz to GHz range) [17,19].

Open-ended coaxial lines are routinely used to characterize the dielectric properties of biological tissues at microwave frequencies [20,21]. Although this method is simple, broadband, and non-destructive, it is not very effective for measuring the properties of solid materials with non-smooth surfaces. In such a situation, the surface roughness and lack of a perfect connection between the probe and the surface of the material under test (caused by the surface roughness) decreases the measurement accuracy.

In this study, we have developed a simple and robust method for measuring the relative dielectric constant and loss tangent of 3D printed materials and demonstrate measurements of three common materials (Acrylonitrile butadiene styrene (ABS), PLA, and Methacrylate Photopolymer Resin (MPR)) used in 3D printing at frequencies relevant to MRI. Our approach utilizes full-wave electromagnetic simulations and scattering parameter measurements of a parallel RLC resonator test fixture measured using a VNA. More specifically, a resonator circuit using the MUT as a parallel plate capacitor is used as a test fixture for material characterization. This technique can cover the necessary MRI frequency ranges of 60 MHz to 300 MHz (for MRI magnetic field strengths of 1.5 T – 7 T) and allows for easy sample preparation, data acquisition, and data analysis. To demonstrate the capability and effects of 3D-printing in designing MRI RF coils, we demonstrate the design and construction of a very low-cost subject and anatomy specific 3D-printed, receive-only RF coil for neck that fits close to the body. We show that the non-flat anatomy-specific coil, which would be challenging to design using conventional approaches, exhibits higher signal-to-noise ratio (SNR) compared to a conventional flat surface coil. Measurements of dielectric constant and loss tangent for 3D-printing materials in our EM simulations were used to achieve an accurate simulation and design of the RF coils.

## Methods

### Material characterization method

Our test fixture is a parallel RLC resonator with resonant frequencies that can be changed within the range of MRI frequencies by choosing an inductor with appropriate value in parallel with the parallel plate capacitor. We printed samples of three distinct 3D printing

materials in the form of rectangular cuboids and used them as the filling dielectric material of the parallel plate capacitor. Figure 1-a shows the printed samples using three different materials (The ABS parts are navy blue, the MPR parts are white, and the PLA parts are Gold/Yellow). Figure 1-b shows the topology of the resonator with the MUT used to construct the parallel plate capacitor. Two series coupling capacitors are used to couple the parallel RLC resonator to the input and output circuits. These series capacitors reduce the loading effects of the  $50 \Omega$  lines connected to the input and output of the resonator on its quality factor. This allows for monitoring small changes in the center frequency and the Q of the resonator from transmission coefficient measurements. Figure 1-c shows the equivalent circuit model of this resonator. Resistive losses of the inductor are modeled as a series resistor. The value of estimated series resistance (ESR) for each inductor is provided in its respective datasheet. The parallel plate capacitor consists of two parts: the ideal capacitor and a fringing capacitor. These two parts provide the total shunt capacitance  $C = C_{MUT} + C_f$  of the resonator. Equations (1) and (2) are the resonant frequency and unloaded quality factor of a parallel RLC resonant circuit, respectively.

$$\omega_r = \frac{1}{\sqrt{L(C_{MUT} + C_f)}} = \frac{1}{\sqrt{LC}} \quad (1)$$

$$Q_{unloaded} = \omega_r \frac{\text{average energy stored}}{\text{energy loss/second}} = \omega_r \frac{W_e + W_m}{P_{loss}} \quad (2)$$

where,  $W_e$  is average electric energy stored in the capacitor,  $W_m$  is the average magnetic energy stored in the inductor,  $P_{loss}$  is the power dissipated by  $R_{loss}$ , and  $\omega_r$  is the resonance frequency.  $R_{loss}$  represents total resonator losses due to conductor loss and dielectric losses in the capacitor dielectric and inductor.

At resonance  $W_e = W_m$  and  $Q_{unloaded} = \omega_r \frac{2W_e}{P_{loss}}$ . For a parallel resonance circuit:

$$Q_{unloaded} = \frac{R_{loss}}{\omega_r L} \quad (3)$$

The unloaded Q defined in equation (3) is a characteristic of the RLC resonator circuit itself, in the absence of any loading effects caused by source and load resistances [22]. When this resonator is directly connected to the external ports of a VNA with  $R_0 = 50 \Omega$ , the quality factor of the resonator changes resulting in the loaded quality factor as defined by equation (4)

$$Q_{loaded} = \frac{R_{total}}{\omega_r L} \quad (4)$$

Where,

$$\frac{1}{R_{total}} = \frac{1}{R_{loss}} + \frac{1}{R_{port1}} + \frac{1}{R_{port2}}$$

As equation (4) shows, the quality factor of the resonator can be significantly decreased if it is directly connected to the input and output transmission lines with characteristic impedances of 50  $\Omega$ . To reduce the loading effect on the measurement, two small capacitors (the coupling capacitors shown in Figure 1-b and 1-c) are used to couple the resonator to the input and output feeding lines. These coupling capacitors increase the effective parallel external impedance that the resonator sees and reduce the impact of the external loading on Q. Because the series impedance that they present is very large, their presence also reduces the magnitude of the transmission coefficient between the input and the output of the resonator. However, this is not a concern as the dynamic range of the VNA is very large and allows us to easily measure the transmission coefficient.

We implemented full-wave electromagnetic simulation model of the resonator in CST Microwave Studio (Computer Simulation Technologies AG, Darmstadt, Germany) taking into account the presence of all the components of the test fixture as well as their material properties (e.g., dielectric loss, thermal, and mechanical properties). Figure 2-a shows the simulated circuit in CST. The red arrows, numbered 1, 2, and 3 are lumped ports used to model the impact of the lumped capacitors and inductor in the full-wave EM simulations. The transmission coefficients of the resonator circuit are calculated using electromagnetic simulations.

Next, transmission coefficient measurements of the resonator were obtained in a range of frequencies containing its resonant frequency using a VNA (N5225A, Keysight Technologies). Scattering parameters of a network describe the magnitude and phase relationships between the incident, transmitted, and reflected waves from the network.  $S_{21}$  is the transmission coefficient for a wave sourced at port 1 and received at port 2. In order to measure  $S_{21}$  of the presented RLC circuit, the two connectors of the circuit are connected to the two ports of the VNA and  $S_{21}$  is measured over the desired frequency range. Figure 2-b shows the fabricated prototype. Figure 2-c shows the measurement setup used to measure the  $S_{21}$  using the VNA. In this arrangement two-port scattering parameters of the parallel RLC resonator circuit were measured using the VNA. Then, using both the magnitude and the phase of the  $S_{21}$  and  $S_{11}$  measurements, the values of the MUT dielectric properties in each simulation model were changed in CST until the best agreement between the simulation and measurement was obtained. This approach was used to characterize the dielectric properties of three commonly-used 3D printed materials (ABS, PLA, and MPR).

### Experimental setup

The resonator circuit was fabricated on a RO4003C substrate (Rogers Corporation), which has well-characterized properties of  $\epsilon_r = 3.38 \pm 0.05$  and  $\tan \delta = 0.0021-0.0027$ . The thickness of the dielectric board was 1.52 mm and the width of the conductor line was 3.7 mm (which was calculated to achieve a characteristic impedance of 50  $\Omega$  for microstrip

lines). The dimensions of the 50  $\Omega$  line impedances were obtained using the LineCalc tool within ADS (Advanced Design System, Keysight Technologies, Santa Rosa, CA), and the properties of the Rogers substrate were as provided by the manufacturer. Samples were rectangular cuboids of size 2.5 cm  $\times$  2.0 cm  $\times$  5 mm. ABS and PLA samples were constructed on a fused deposition modeling (FDM) 3D printer (Ultimaker Extended 2+). The MPR sample was constructed on a Stereolithography (SLA) 3D printer (Formlabs Form 2). These samples, shown in Figure 1-a, were used as the insulator between two layers of copper tape (thickness: 0.07 mm) as conductive elements to create parallel plate capacitors in parallel with an inductor in a RLC resonant circuit. The characteristics of the inductors used in the circuits are: 1) L = 554.28 nH (Coilcraft 132-20SM) with Q = 149 at 64 MHz, ESR = 1.51  $\Omega$ , and self-resonance frequency (SRF) = 490 MHz, 2) L = 175.57 nH (Coilcraft 132-12SM) with Q = 169 at 128 MHz, ESR = 0.025  $\Omega$ , and SRF = 875MHz, 3) L = 82 nH (Coilcraft 1812SMS-82N) with Q = 151 at 300 MHz, ESR = 0.0094  $\Omega$ , and SRF = 1.3 GHz. As described above, two 1 pF capacitors (S603DS, Johnson Technology) were used as the coupling capacitors. We fabricated five samples from each material to minimize the influence of printing inaccuracies, connectors, and parasitic losses on the overall measurement. To test and validate the accuracy of our method, a sample with a known permittivity (Rogers Corporation 6010 board) was characterized first.

### Estimation of dielectric properties without EM simulations

Complex permittivity can also be estimated based on the change of the resonant frequency and quality factor by replacing the sample with one that has known parameters. With this change, relative dielectric constant  $\epsilon_r'$  and loss tangent  $\epsilon_r''$  can be calculated respectively.

**Extraction of  $\epsilon_r'$** —The series branch  $R_0$ ,  $C_{coupling}$  in Figure 1-c, can be turned into an effective parallel  $R_p$  and  $C_p$ . This is shown in Figure 3-a. The values of parallel components can be calculated using following equations. This is also shown in Figure 3-b.

$$R_p = R_0(1 + Q_s^2) \approx R_0 Q_s^2 \quad X_{C_p} = X_{C_{coupling}} \frac{1 + Q_s^2}{Q_s^2} \approx X_{C_{coupling}} \quad (5)$$

Where,  $Q_s = \frac{X_{C_{coupling}}}{R_0}$  and  $X_{C_{coupling}}$  is the reactance value of coupling capacitor. Since the total capacitance is now  $C_{MUT} + C_f + 2C_{coupling}$ . The resonance frequency of this circuit is:

$$\omega_r = \frac{1}{\sqrt{L(C_{MUT} + C_f + 2C_{coupling})}} \quad (6)$$

And  $C_{MUT} = f(L, \omega_r, C_{coupling}, C_f) = \frac{1}{L} \omega_r^{-2} - (2C_{coupling} + C_f)$ .

Electromagnetic simulations already take the fringing effects of a parallel plate capacitor and MUT thickness into account. Therefore, it is important to consider these parameters in calculations. The capacitance of a rectangular or square parallel plate capacitor including the fringing effect, can be calculated using the following formula [23]:

$$C = \frac{0.0885 \times \epsilon'_r (L + \Delta u)(W + \Delta u)}{d} \quad \Delta u = d + \frac{0.0885 \times 10 \times d \times \ln((L \times W) + 1)}{\pi} \quad (7)$$

$C_{MUT}$  can be calculated using measurements of frequency of the peak of  $S_{21}$  ( $\omega_r$ ) for both a known sample and the MUT. Note that  $C_f$  can vary between known sample and MUT due to different sample size and thickness.

$$C_{MUT} = C_{KnownSample} * \frac{f_{MUT}(L, \omega_r, C_{coupling}, C_f)}{f_{KnownSample}(L, \omega_r, C_{coupling}, C_f)} \quad (8)$$

$\epsilon'_{rMUT}$  can be calculated using  $C_{MUT}$  using equation (7).

**Extraction of  $\tan\delta$** —The  $Q$  factor of the circuit is:

$$\frac{1}{Q} = \frac{1}{Q_u} + \frac{1}{Q_c} \quad (9)$$

where,  $Q_c$  is the external  $Q$  induced by the coupling capacitors and the ports and can be

expressed as  $Q_c = \frac{R_p/2}{\omega_r L} = \frac{Q_s^2 R_0}{2\omega_r L}$ .  $Q_u$  is the unloaded internal  $Q$  of the circuit without the external series branches. The unloaded  $Q$  can be written as

$$\frac{1}{Q_u} = \frac{1}{Q_L} + \frac{1}{Q_{RMUT}} \quad (10)$$

$Q_L$  corresponds to the losses in the series resistor of the inductor ( $r_L$ ), in other word it is the

quality factor of the inductor at  $\omega_r$  and is defined as  $Q_L = \frac{\omega_r L}{r_L}$ . The value of this  $Q$  is specified in the inductors datasheet by the manufacturer.  $Q_{RMUT}$  corresponds to the losses in

MUT and defined as  $Q_{RMUT} = \frac{R_{MUT}}{\omega_r L}$ . The total  $Q$  is then:

$$\frac{1}{Q} = \frac{1}{Q_L} + \frac{1}{Q_c} + \frac{1}{Q_{RMUT}} \quad (11)$$

$Q$  can be measured using S-parameter measurements of the circuit using:

$$Q = \frac{f_r}{f_{r(3dB)}} \quad (12)$$

By measuring  $Q$ , we can calculate  $Q_{R_{MUT}}$  and respectively  $R_{MUT}$ . In a parallel plate capacitor with lossy material modeled as a parallel RC, admittance can be written as:

$$Y = \frac{1}{Z} = j \frac{\omega \varepsilon_0 \varepsilon_r A}{d} = \frac{j \omega \varepsilon_0 (\varepsilon_r' - j \varepsilon_r'') A}{d} = \frac{j \omega \varepsilon_0 \varepsilon_r' A}{d} + \frac{\omega \varepsilon_0 \varepsilon_r'' A}{d} \quad C = \frac{\varepsilon_0 \varepsilon_r' A}{d}, G = \frac{1}{R} = \frac{\omega \varepsilon_0 \varepsilon_r'' A}{d}, \tan \delta = \frac{\varepsilon_r''}{\varepsilon_r'} \quad (13)$$

Since  $\tan \delta \propto R_{MUT}^{-1}$ , and  $R_{MUT} \propto Q_{R_{MUT}}$ , we can write:

$$\tan \delta_{MUT} = \tan \delta_{KnownSample} \frac{Q_{KnownSample}}{Q_{MUT}} \times \frac{\varepsilon_r'_{KnownSample}}{\varepsilon_r'_{MUT}} \quad (14)$$

Where,  $Q_{KnownSample} = \left( \frac{1}{Q_{Measured-KnownSample}} - \left( \frac{1}{Q_L} + \frac{1}{Q_C} \right) \right)^{-1}$ , and

$$Q_{MUT} = \left( \frac{1}{Q_{Measured-MUT}} - \left( \frac{1}{Q_L} + \frac{1}{Q_C} \right) \right)^{-1}$$

Using equations (8) and (14), we estimated the dielectric constant and loss tangent of the 3D-printed materials using a known sample of Rogers 6010 ( $\varepsilon_r' = 10.7$ ,  $\tan \delta = 0.0023$ ).

## RF coil design

To demonstrate the use of 3D printing material characterization data to simulate and design MRI receive coils, two MRI receive-only coils were simulated and constructed for imaging cervical spine. Both coils were constructed on a FDM 3D printer (Ultimaker Extended 2+) from PLA polymer both because of its low loss tangent at 127.8 MHz (3T MRI) and good stability during 3D printing compared to other materials. Here, we 3D-printed the frame and support structure of the coils and added copper tape and other circuit components to complete the design of the coil. The first coil is a conventional, flat single-channel surface coil. The other coil is designed in a way that fits against the neck and is close to the body. To design the anatomy specific coil, one subject was recruited and provided informed consent under an appropriate IRB protocol. MR images of the volunteer were obtained (3D Gradient Echo, TE= 1.8 ms, TR= 4.3 ms, spatial resolution: 0.78×0.78×1 mm) from which a 3D CAD model of volunteer head and neck was created. This 3D model was used as input to the EM simulation in CST to design a specific neck coil for the volunteer. Figure 4-a shows the EM

simulation environment. The material properties of the support structure in the simulation are those calculated with our test fixture for PLA. Figure 4-b shows the simulated and constructed anatomy-specific coil. Figure 4-c shows the flat surface coil. Both coils have the same diameter and utilize a path in their support structure for the resonant loop as negative relief. Conductive elements of both loops are 6-mm wide, 0.07-mm thick copper tape. The coils inductances were calculated using full-wave EM simulation and the component values for matching and tuning networks were optimized in CST Design Studio (CST DS). Coils were matched to  $50 \Omega$  and tuned to 127.8 MHz (3T MRI). A detuning circuit was designed for each coil to detune the coil and prevent interactions between the loop coil with the body transmit coil. When the PIN diode (UMX5101, Microsemi, Aliso Viejo, CA) used in detuning circuit is forward biased with sufficient DC current, it makes a short circuit and makes the inductor  $L_d$  resonate in parallel with the capacitor  $C_t$  presenting a very high impedance at the desired frequency and open circuit the loop [24]. The matching/detuning network was fabricated on FR4 substrate (Circuit Specialist, Tempe, AZ). The components used for the tuning/matching network consist of fixed non-magnetic capacitors (Johnson Manufacturing), one variable capacitor (Johnson Manufacturing, JMC80H85), and fixed non-magnetic inductors (Coilcraft 132 series). Figure 4-d shows the circuit diagram of the tuning, matching, and detuning network.

## Imaging

Imaging was performed on both MR spherical phantom and the volunteer neck. A custom-built gateway (Clinical MR Solutions, Brookfield, WI) provides integration to the 3T MRI scanner (Signa PET/MR, GE Healthcare, Waukesha, WI) and includes a BNC connection, a low-noise preamplifier, and active decoupling circuitry. MR sequence parameters for the phantom imaging included: pulse sequence= 2D spin echo, TE= 20 ms, TR= 750 ms, spatial resolution=  $0.94 \times 0.94 \times 3$  mm. MR sequence parameters for in vivo imaging of the volunteer's neck included: pulse sequence= 2D fast spin echo, TE= 9.2 ms, TR= 800 ms, ETL= 3, spatial resolution=  $0.7 \times 1.1 \times 4$  mm.

## Results

### Validation

To test and validate our simulation model, a sample with a known permittivity (Rogers corporation 6010 board) was used to validate the accuracy of the method. The resulting extracted dielectric properties for Rogers 6010 were  $\epsilon_r = 10.66$  and the  $\tan \delta = 0.0018$  for the frequency range of operation. The manufacturer specifies values of  $\epsilon_r = 10.7$  for design dielectric constant and  $\tan \delta = 0.0023$  for frequencies up to 10 GHz. This high level of agreement in the dielectric properties confirms the validity of our model and approach.

### 3D printing material dielectric properties

Figure 5 shows the simulation and measurement transmission coefficients of the resonator approximately tuned to the 7T MRI frequency for extracting the material properties of PLA at this frequency. The very good agreement between the measurement and simulation results confirms the validity of the model used in the full-wave EM simulations. Figure 6 shows the measured magnitudes of the transmission coefficients of three different resonators tuned to

operate at the 1.5T MRI frequency ( $63 \text{ MHz} \pm 7 \text{ MHz}$ ). The resonators use parallel plate capacitors filled with different 3D printed materials. Since all other components of the circuit except the parallel plate capacitor remained unchanged in the measurements, the differences in the resonant frequencies (the frequency where the peak of  $S_{21}$  happens) is related to the difference in the dielectric constant of the material. Additionally, the change in the resonator Q and its loss, as evidenced by the reduction of the magnitude of the  $S_{21}$  and the broadening of the 3-dB bandwidth of the resonator, can be attributed to the losses of the 3D printed dielectrics filling the volume within the parallel plate capacitors. It can be seen that the dielectric constant of photopolymer resin is higher than those of the ABS and PLA. Also, the photopolymer resin has higher dielectric loss than ABS and PLA.

Figure 7 shows the extracted dielectric properties (dielectric constant and loss tangent) for these three commonly-used 3D printing materials using the proposed resonator for common MRI RF frequencies. These estimated properties (dielectric constant/loss tangent) were:  $3.11 \pm 0.07/0.013 \pm 0.001$  for PLA,  $3.18 \pm 0.06/0.012 \pm 0.003$  for ABS, and  $4.11 \pm 0.06/0.025 \pm 0.002$  for photopolymer resin at 63 MHz. Measurement variability is attributed to small differences in the printing processes for each of the samples used to extract these properties.

Dielectric properties of 3D-printed materials were also estimated from only analytical equations using the developed method. A comparison of EM simulation results and analytical result are provided in Table 1. Although electromagnetic simulations consider all the parasitic effects and elements that are not considered in the analytical equations and calculations, the analytical approach can provide a good estimate for a quick calculation and comparison between different materials.

To our knowledge, no other reports in the literature have described the dielectric properties of 3D printed materials at MRI-relevant frequency ranges. There are however, studies on these materials in other frequency ranges. A comparison of the dielectric constant and loss tangent measured with the authors' method and published literature is provided in Table 2.

### RF coil design and imaging

Figure 8-a shows the measured reflection coefficients of the coils. Both coils have a similar quality factor of approximately 40. Figure 8-b shows the MR images of the phantom scanned using the two 3D printed coils. Figure 8-c shows the region of interest (ROI) for calculating the SNR, calculated using National Electrical Manufacturers Association (NEMA) method with two images acquired by consecutive scans. The SNR in this region for the anatomy-specific coil was 394 compared to the flat surface coil which was 293. Figure 9 shows the cervical spine images of the volunteer show a higher SNR when using the anatomy-specific neck coil placed against the neck.

### Discussion

The use of additive manufacturing in the development of MRI devices is highly appealing. By providing great flexibility in the design and fabrication of structural components, different 3D geometries can be quickly designed and printed for evaluation until the design is optimized. For MRI coils, 3D printing is a helpful tool for making arbitrary 3D geometries

that are challenging to build by traditional manufacturing methods (using hand or lithography techniques). Furthermore, with high precision 3D printers that have resolution well below 100 microns becoming commonplace, the realized outputs match very closely to the original design, allowing a natural translation of increased reliance on 3D simulation to improve coil design and reduce construction time. Finally, given the relatively low production quantities of MRI coils relative to common consumer goods, it could be expected that the field will see an increased reliance on these technologies not only for research developments, but potentially for coil structures and components used for clinical imaging.

For 3D-printed structures to be robustly introduced into a computational design and simulation regime, the electrical properties of the 3D printing material are required design parameters. Characterizing the dielectric properties helps determine the optimal material with lowest dielectric loss and desired dielectric constant. In RF and antenna design and specifically in designing MRI RF coils, it is important to use low loss materials to decrease total loss in the signal path, increase SNR, and increase the minimum detectable signal. Based on the results of dielectric properties of the three common 3D printing materials we characterized, ABS and PLA are better choices for RF design than photopolymer resin for designing MRI coils.

We have developed a test fixture using parallel plate capacitors developed from 3D printed materials and a resonant RLC circuit. We demonstrated measurements conducted with this fixture with three different commonly utilized 3D printing materials and utilized these measurements in EM simulations to design two PLA-printed coils. The benefit of such a test fixture is that it is easy to construct, is low cost, and may be used to measure material properties across the range of frequencies relevant to MRI. Given the wide variety of material types available for FDM, SLA, and other 3D printing technologies with a large number of vendors and little to no standardization of materials, it is feasible to perform testing on each material using this technique, should an accurate characterization be necessary. To our knowledge, no test fixtures have been described in the literature that enable the testing of 3D printed materials at MRI-relevant frequency ranges.

We demonstrated a method for the construction of anatomy-specific 3D-printed MR coils that can provide the improved SNR for imaging a specific area of body. These coils can be designed and implemented very quickly with a very low cost for each body region (and potentially for each patient). The coil demonstrated herein used inexpensive components, including the resonant structure, which was formed from 6-mm copper tape into the 3D printed substrate. Other components were low cost, and only one tunable capacitor was required to provide frequency tuning of the coil.

In summary, we have demonstrated a new technique to characterize 3D printed materials and have used that characterization to optimize the EM design of an application specific MR RF coil. In particular, this flexibility of computer design and additive manufacturing of MRI RF coils can be beneficial for the application of MR-based radiation therapy planning and in particular with the increasing availability of combined MR-Linac scanners, where anatomy and subject-specific coils could be created to perform optimal imaging (and/or treatment) in the therapy position.

## Acknowledgments

The project described was supported in part by NIH UL1TR000427 and DARPA N66001-17-2-4010. The content is solely the responsibility of the authors.

## References

- Herrmann KH, Gärtner C, Güllmar D, Krämer M, Reichenbach JR. 3D printing of MRI compatible components: Why every MRI research group should have a low-budget 3D printer. *Med Eng Phys*. 2014; 36:1373–1380. DOI: 10.1016/j.medengphy.2014.06.008 [PubMed: 25092622]
- Wei S, Wang Z, Wang H, Lyu X, Deng L, Yang W. Design and implementation of MRI RF coil based on 3D printing. 2015 IEEE MTT-S 2015 Int Microw Work Ser RF Wirel Technol Biomed Healthc Appl IEEE. 2015; :222–224. DOI: 10.1109/IMWS-BIO.2015.7303857
- Rigla JP, Sarwar A, Nacev A, Urdaneta MG, Anashkin E, Stepanov P, Weinberg IN, Benlloch JM, McMillan A, Hilaman R, Fricke ST. Design and additive manufacturing of MRI gradient coils. 2014 IEEE Nucl Sci Symp Med Imaging Conf, IEEE. 2014; :1–4. DOI: 10.1109/NSSMIC.2014.7430974
- Corea JR, Lechene PB, Lustig M, Arias AC. Materials and methods for higher performance screen-printed flexible MRI receive coils. *Magn Reson Med*. 2017; 78:775–783. DOI: 10.1002/mrm.26399 [PubMed: 27612330]
- Corea JR, Flynn AM, Lechêne B, Scott G, Reed GD, Shin PJ, Lustig M, Arias AC. Screen-printed flexible MRI receive coils. *Nat Commun*. 2016; 7:10839.doi: 10.1038/ncomms10839 [PubMed: 26961073]
- Wang S, Duyn JH. Time-domain finite-difference/finite-element hybrid simulations of radio frequency coils in magnetic resonance imaging. *Phys Med Biol*. 2008; 53:2677–2692. DOI: 10.1088/0031-9155/53/10/016 [PubMed: 18445873]
- Giovannetti G, Tiberi G, Tosetti M. Finite element method-based approach for radiofrequency magnetic resonance coil losses estimation. *Concepts Magn Reson Part B Magn Reson Eng*. 2016; 46B:e21348.doi: 10.1002/cmr.b.21348
- Kozlov M, Turner R. Fast MRI coil analysis based on 3-D electromagnetic and RF circuit co-simulation. *J Magn Reson*. 2009; 200:147–152. DOI: 10.1016/j.jmr.2009.06.005 [PubMed: 19570700]
- Chen, L., ONG, CK., Neo, CP., Varadan, VV., Varadan, VK. *Electromagnetic properties of materials*. Vol. 1. John Wiley; 2004. Microwave electronics: measurement and materials characterisation; p. 1-28.
- Deffenbaugh PI, Rumpf RC, Church KH. Broadband Microwave Frequency Characterization of 3-D Printed Materials. *IEEE Trans Components, Packag Manuf Technol*. 2013; 3:2147–2155. DOI: 10.1109/TCPMT.2013.2273306
- Baker-Jarvis J, Janezic M, Degroot D. High-frequency dielectric measurements. *IEEE Instrum Meas Mag*. 2010; 13:24–31. DOI: 10.1109/MIM.2010.5438334
- Aguilar SM, Shea JD, Al-Joumayly MA, Van Veen BD, Behdad N, Hagness SC. Dielectric Characterization of PCL-Based Thermoplastic Materials for Microwave Diagnostic and Therapeutic Applications. *IEEE Trans Biomed Eng*. 2012; 59:627–633. DOI: 10.1109/TBME.2011.2157918 [PubMed: 21622068]
- Barot SF, Bernhard JT. Permittivity measurement of layered media using a microstrip test bed. 2008 IEEE Antennas Propag Soc Int Symp IEEE. 2008; :1–4. DOI: 10.1109/APS.2008.4619797
- Barry W, Broad-Band A. Automated, Stripline Technique for the Simultaneous Measurement of Complex Permittivity and Permeability. *IEEE Trans Microw Theory Tech*. 1986; 34:80–84. DOI: 10.1109/TMTT.1986.1133283
- Ghodgaonkar DK, Varadan VV, Varadan VK. Free-space measurement of complex permittivity and complex permeability of magnetic materials at microwave frequencies. *IEEE Trans Instrum Meas*. 1990; 39:387–394. DOI: 10.1109/19.52520
- Aris MAB, Ghodgaonkar DK. Nondestructive and noncontact dielectric measurement method for high-loss liquids using free space microwave measurement system in 8 - 12.5 GHz frequency

- range. 2004 RF Microw Conf (IEEE Cat No.04EX924) IEEE. :169–176. n.d. DOI: 10.1109/RFM.2004.1411102
17. Boybay MS, Ramahi OM. Material Characterization Using Complementary Split-Ring Resonators. IEEE Trans Instrum Meas. 2012; 61:3039–3046. DOI: 10.1109/TIM.2012.2203450
  18. Milovanovic B, Ivkovic S, Tasic V. A simple method for permittivity measurement using microwave resonant cavity. 12th Int Conf Microwaves Radar MIKON-98 Conf Proc (IEEE Cat No. 98EX195) Telecommun Res Inst. :705–709. n.d. DOI: 10.1109/MIKON.1998.742809
  19. Baker-Jarvis J, Geyer RG, Grosvenor JH, Janezic MD, Jones CA, Riddle B, Weil CM, Krupka J. Dielectric characterization of low-loss materials a comparison of techniques. IEEE Trans Dielectr Electr Insul. 1998; 5:571–577. DOI: 10.1109/94.708274
  20. Popovic D, McCartney L, Beasley C, Lazebnik M, Okoniewski M, Hagness SC, Booske JH. Precision open-ended coaxial probes for in vivo and ex vivo dielectric spectroscopy of biological tissues at microwave frequencies. IEEE Trans Microw Theory Tech. 2005; 53:1713–1722. DOI: 10.1109/TMTT.2005.847111
  21. Ganchev SI, Qaddoumi N, Bakhtiari S, Zoughi R. Calibration and measurement of dielectric properties of finite thickness composite sheets with open-ended coaxial sensors. IEEE Trans Instrum Meas. 1995; 44:1023–1029. DOI: 10.1109/19.475149
  22. Pozar, DM. Microwave engineering, Microwave resonators. Vol. 6. Wiley; 2012. p. 272-278.
  23. Hosseini M, Zhu G, Peter YA. A new formulation of fringing capacitance and its application to the control of parallel-plate electrostatic micro actuators. Analog Integr Circuits Signal Process. 2007; 53:119–128. DOI: 10.1007/s10470-007-9067-3
  24. Nilsson DTP, Mohr JJ, Zhurbenko V. Practical aspects of 13C surface receive coils with active decoupling and tuning circuit. 2012 42nd Eur Microw Conf, IEEE. 2012; :65–68. DOI: 10.23919/EuMC.2012.6459403
  25. Shinyama K, Fujita S. Study on the electrical properties of a biodegradable plastic. Proc 7th Int Conf Prop Appl Dielectr Mater (Cat No.03CH37417) IEEE. :707–710. n.d. DOI: 10.1109/ICPADM.2003.1218515
  26. Dichtl C, Sippel P, Krohns S. Dielectric Properties of 3D Printed Polylactic Acid. Adv Mater Sci Eng. 2017; 2017:1–10. DOI: 10.1155/2017/6913835
  27. Huber E, Mirzaee M, Bjorgaard J, Hoyack M, Noghianian S, Chang I. Dielectric property measurement of PLA. 2016 IEEE Int Conf Electro Inf Technol, IEEE. 2016; :0788–0792. DOI: 10.1109/EIT.2016.7535340
  28. Felicio JM, Fernandes CA, Costa JR. Complex permittivity and anisotropy measurement of 3D-printed PLA at microwaves and millimeter-waves. 2016 22nd Int Conf Appl Electromagn Commun, IEEE. 2016; :1–6. DOI: 10.1109/ICECom.2016.7843900
  29. Riddle B, Baker-Jarvis J, Krupka J. Complex permittivity measurements of common plastics over variable temperatures. IEEE Trans Microw Theory Tech. 2003; 51:727–733. DOI: 10.1109/TMTT.2003.808730
  30. Thomas P, Ravindran RSE, Varma KBR. Dielectric properties of Poly(methyl methacrylate) (PMMA)/CaCu<sub>3</sub>Ti<sub>4</sub>O<sub>12</sub> composites. 2012 IEEE 10th Int Conf Prop Appl Dielectr Mater, IEEE. 2012; :1–4. DOI: 10.1109/ICPADM.2012.6319009

### Highlights

- A method to characterize the dielectric constant and loss tangent of 3D printed materials at relevant MR frequencies is proposed.
- The method relies on full-wave electromagnetic simulations.
- The design and construction procedure of a very low-cost subject/anatomy-specific 3D printed receive-only RF coil is provided.

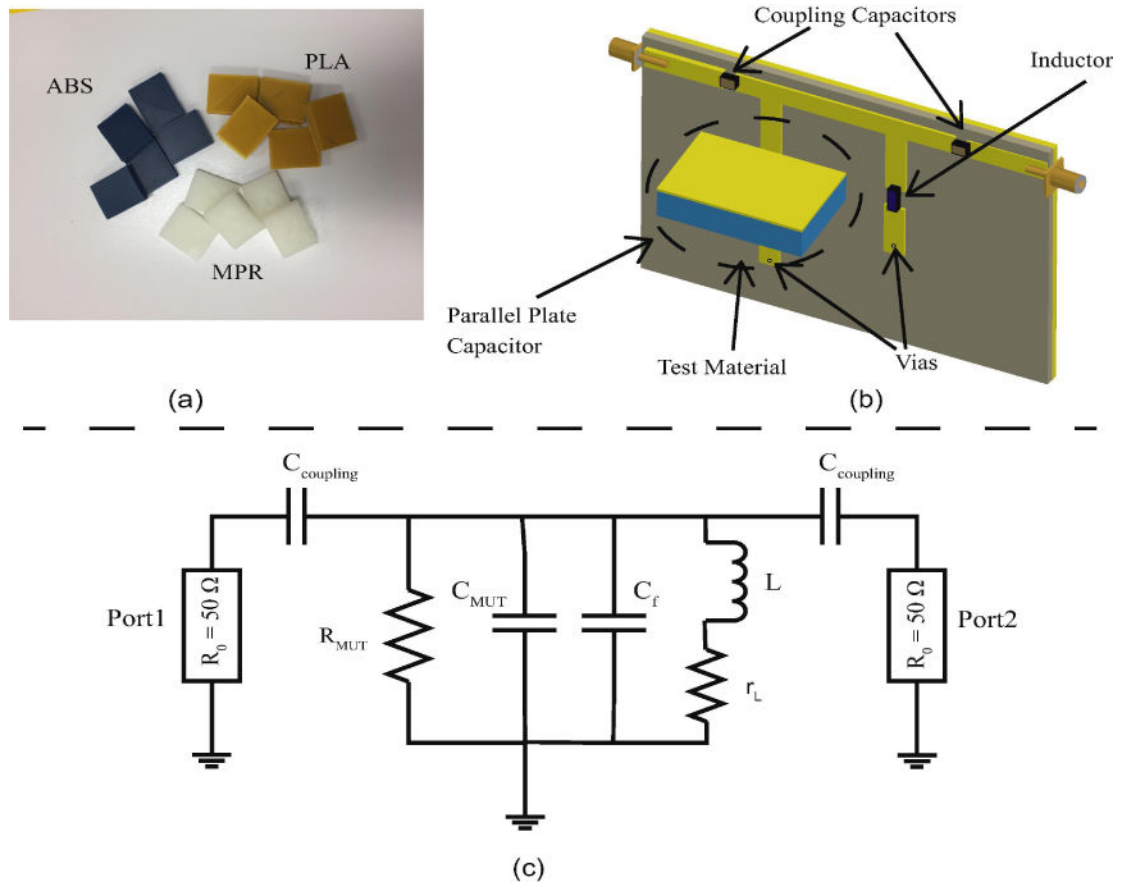


**Figure 1.** Parallel RLC resonator (a) printed samples using three different materials (The ABS parts are navy blue, the MPR parts are white, and the PLA parts are Gold/Yellow), (b) topology of the resonator, (c) the equivalent circuit model of this resonator.

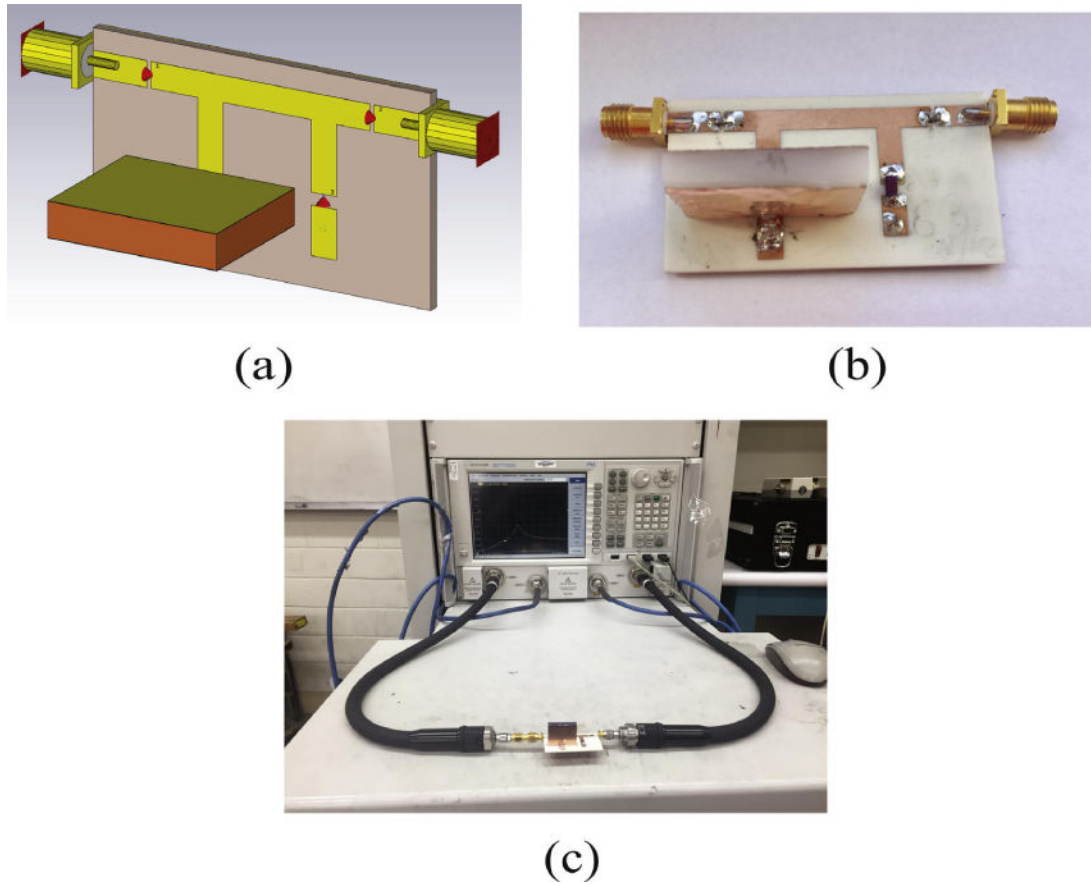


**Figure 2.**

(a) simulated parallel RLC resonant circuit in CST. The red arrows, numbered 1, 2, and 3 are lumped ports used to model the impact of the lumped capacitors and inductor in the full-wave EM simulations. (b) fabricated test fixture, (c) measurement setup used to measure the  $S_{21}$  (transmission coefficient) using a VNA.

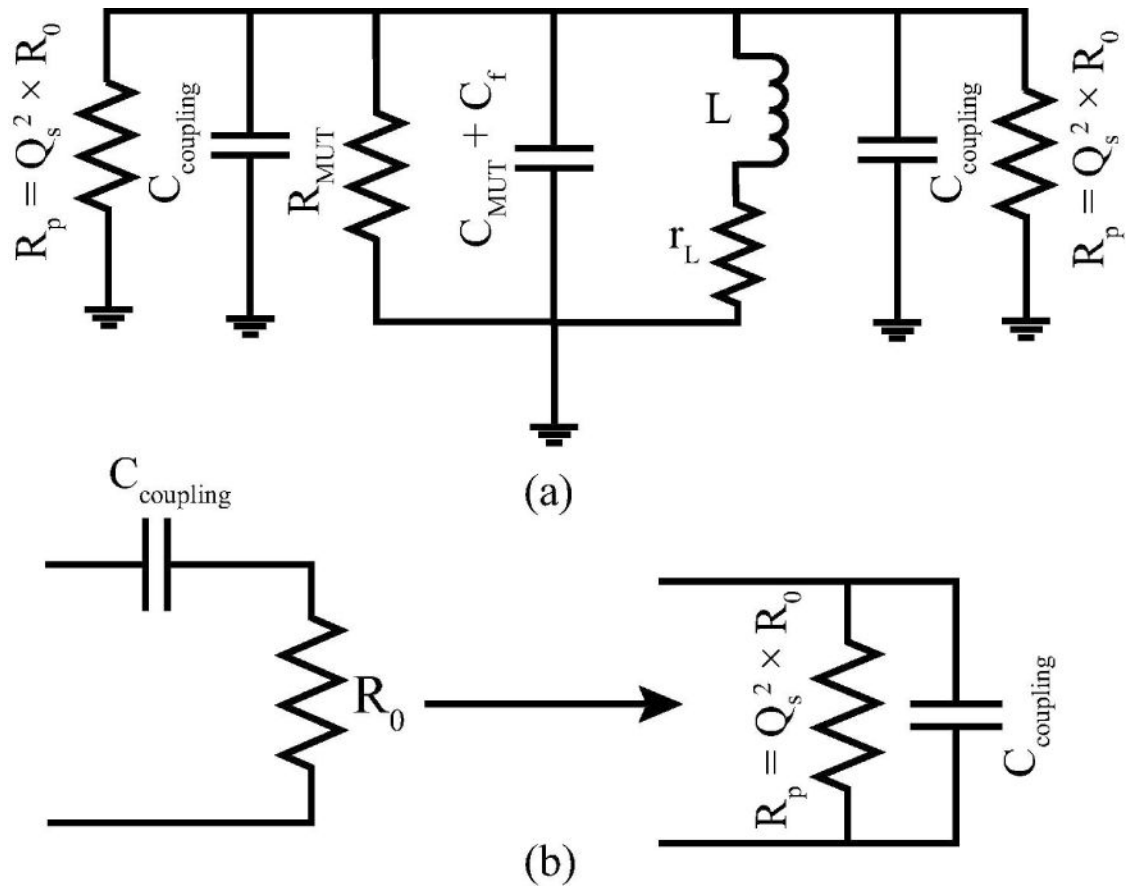


**Figure 3.** (a) equivalent circuit model with series to parallel conversion. (b) series to parallel conversion.

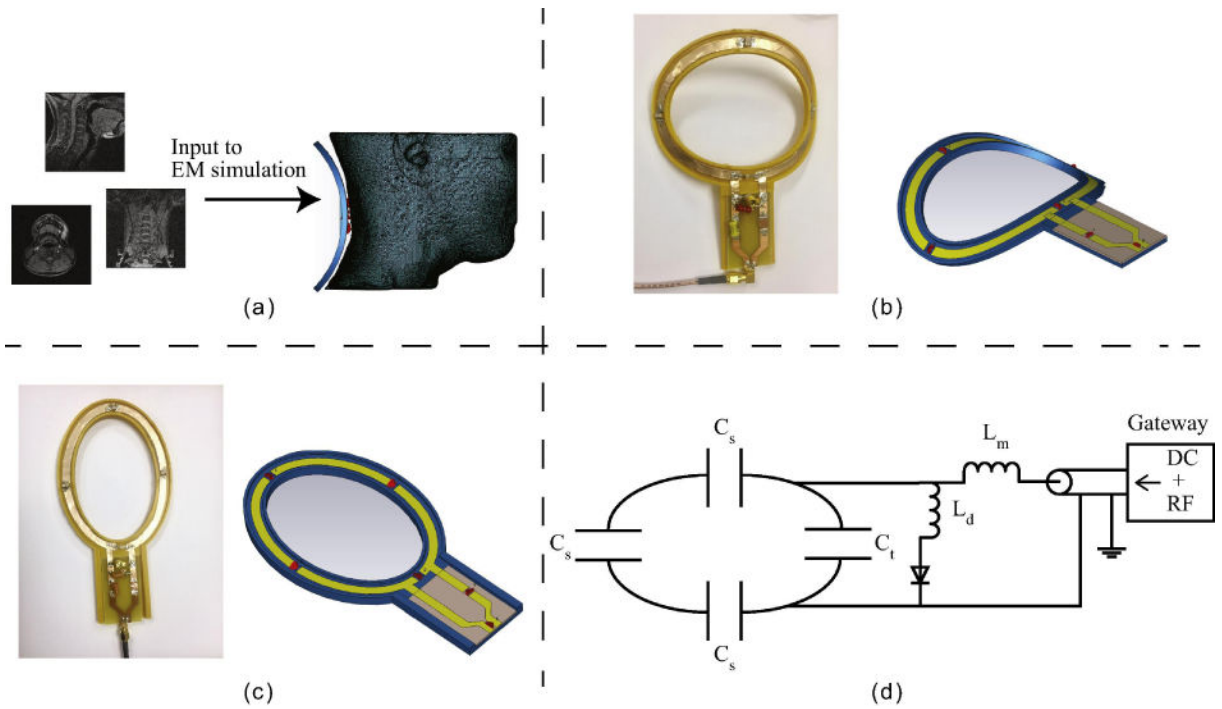


**Figure 4.**

(a) Design procedure and EM simulation of anatomy specific coil. (b) Simulated and constructed anatomy specific coil. (c) simulated and constructed flat coil. (d) the circuit diagram of the tuning, matching, and detuning network.

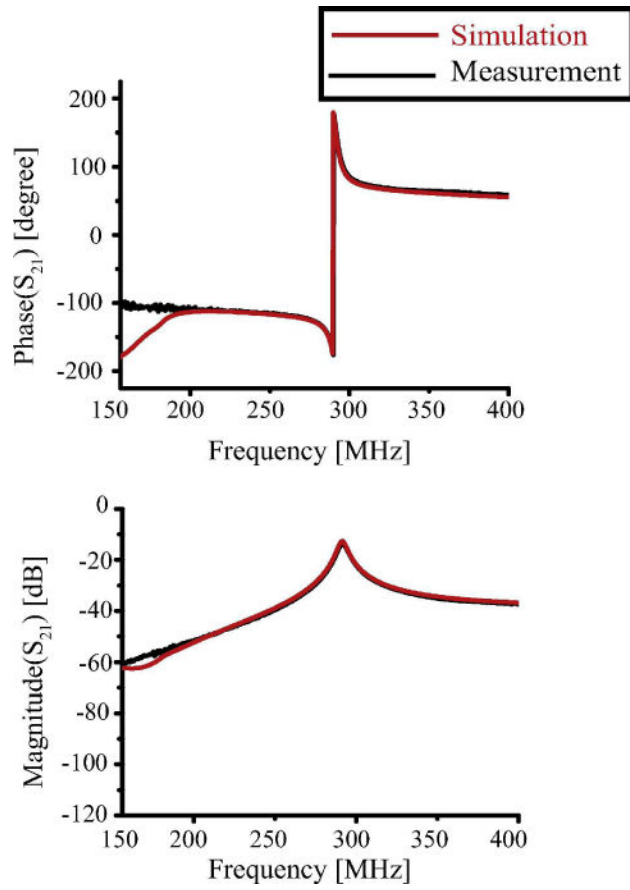


**Figure 5.** Simulation and measurement transmission coefficients of the resonator approximately tuned to the 7 T MRI frequency using PLA as MUT.

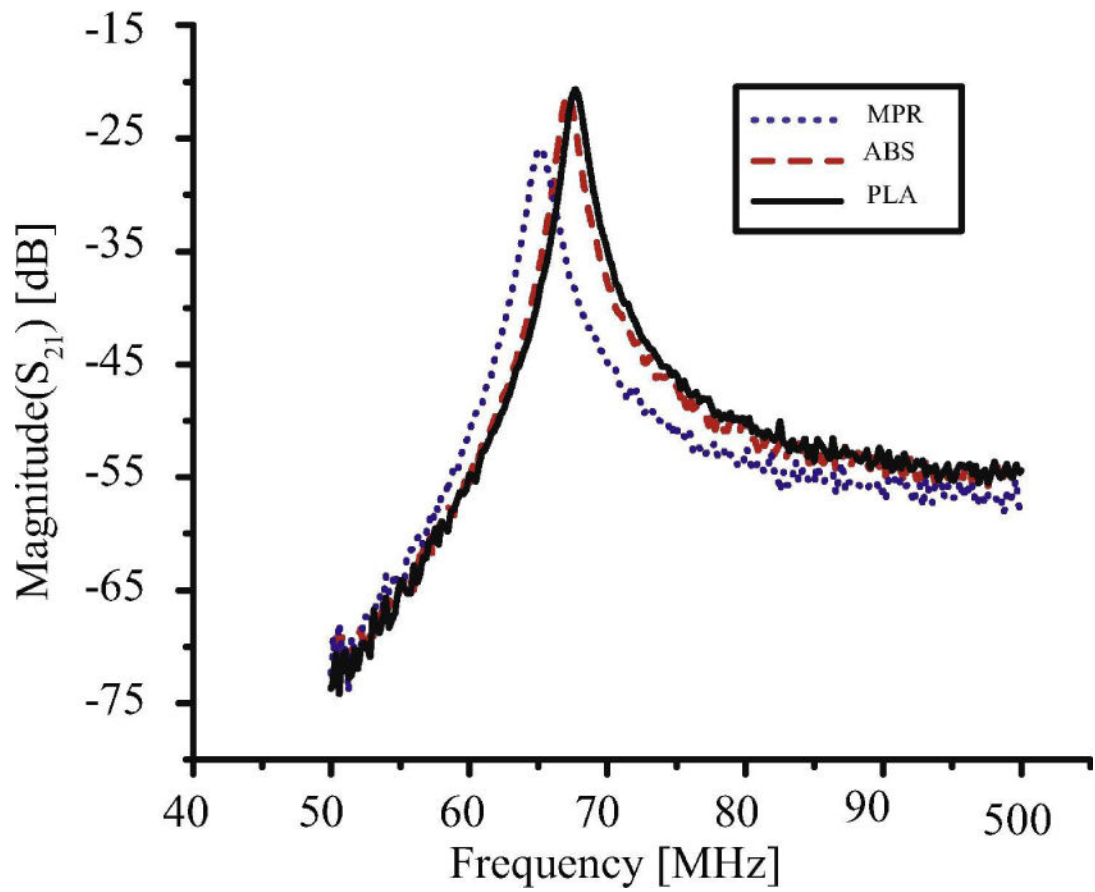


**Figure 6.** Measured magnitudes of the transmission coefficients of the resonator tuned to operate at the 1.5 T MRI frequency with three different MUT.

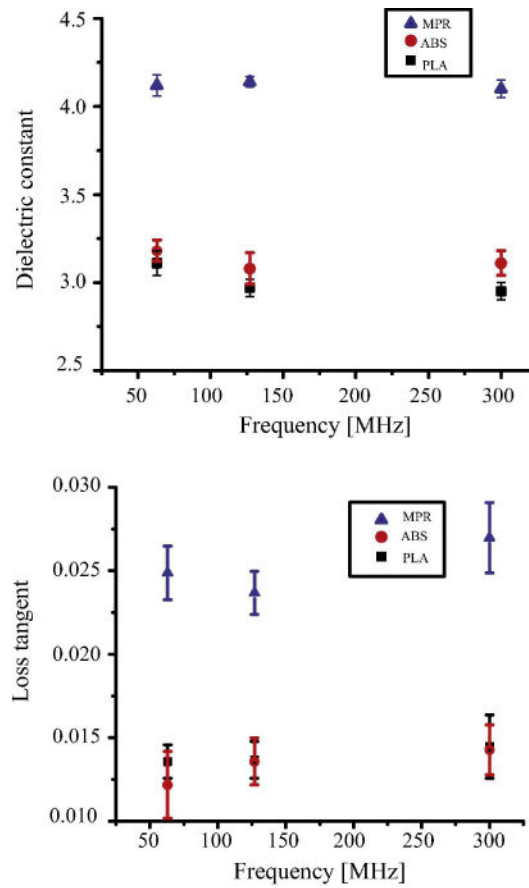


**Figure 7.** Extracted dielectric properties (dielectric constant and loss tangent) for three commonly-used 3D printing materials (ABS, PLA, MPR) using the proposed resonator for common MRI RF frequencies.

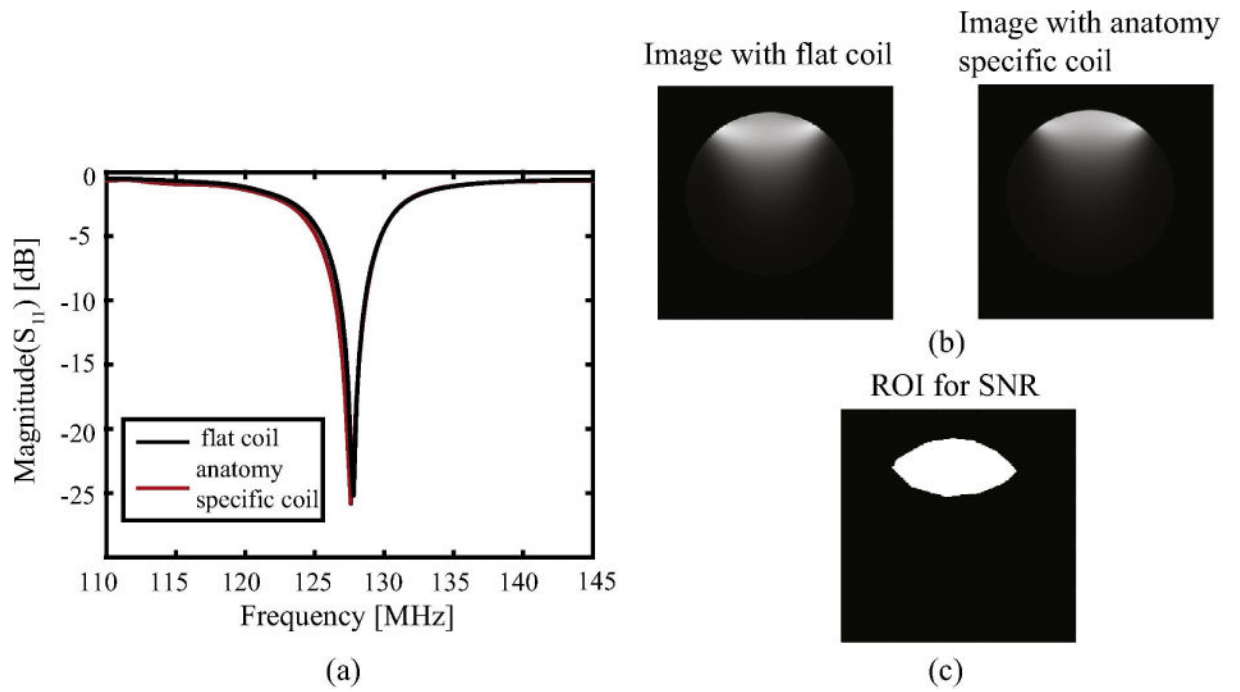


**Figure 8.** (a) measured reflection coefficients of the two coils (b) MR images of the phantom (c) ROI for calculating the SNR.

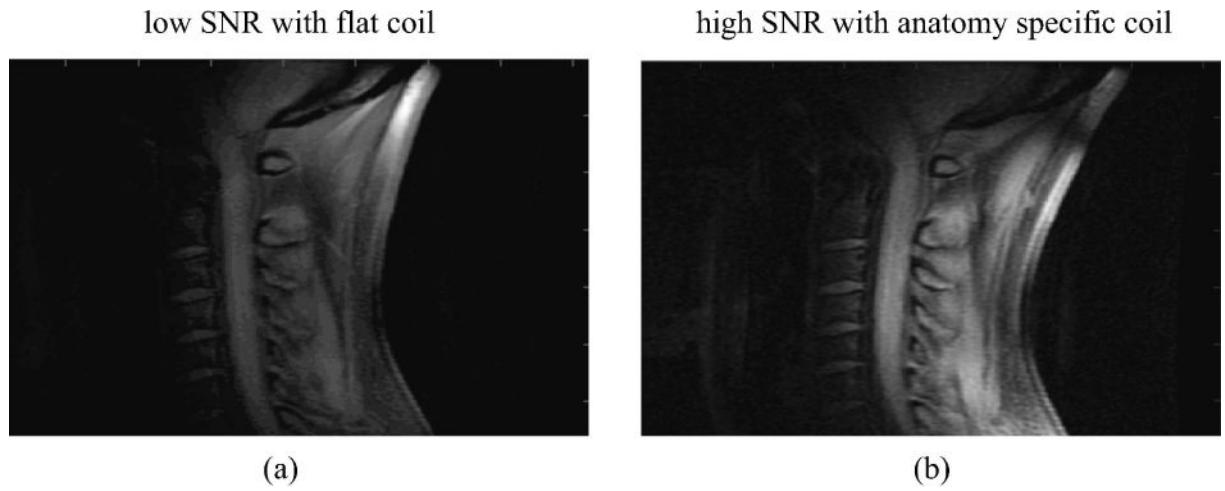


**Figure 9.** Cervical spine images of the volunteer showing (a) low SNR when using a flat coil and (b) high SNR when using the anatomy-specific neck coil placed against the neck.

Comparison of measured dielectric constant and loss tangent of 3D-printed materials using EM simulations and estimated parameters using analytical method.

**Table 1**

Frequency (MHz)	ABS		PLA		MPR			
	$\epsilon_r'$	$\tan\delta$	$\epsilon_r'$	$\tan\delta$	$\epsilon_r'$	$\tan\delta$		
63	Analytical approach		2.92	0.015	2.90	0.017	3.73	0.029
	EM simulation		3.18	0.012	3.11	0.013	4.11	0.025
128	Analytical approach		3.21	0.014	3.17	0.017	3.68	0.028
	EM simulation		3.08	0.013	2.98	0.013	4.12	0.023
300	Analytical approach		2.89	0.018	2.85	0.016	3.84	0.031
	EM simulation		3.11	0.014	2.95	0.014	4.10	0.027

**Table 2**

Published literature on measuring dielectric constant and loss tangent of 3D-printed materials

PLA	Frequency	$\epsilon_r'$	$\tan\delta$
[25]	1 KHz 100 KHz	2.46–2.59 2.43–2.65	$(2.6-3) \times 10^{-3}$ $(4.9-9) \times 10^{-3}$
[26]	1Hz - 3GHz	2.1–2.9	$(1 \pm 0.2) \times 10^{-2}$
[27]	9–10 GHz	3.549	$(1.1 \pm 0.2) \times 10^{-2}$
[28]	40GHz	$2.75 \pm 0.05$	$(1.1 \pm 0.2) \times 10^{-2}$
Proposed method	63MHz	3.11	0.013
	128MHz	2.98	0.013
	300 MHz	2.95	0.014
ABS	Frequency	$\epsilon_r'$	$\tan\delta$
[10]	0.01-10 GHz	2.54–2.83	$(0.6-1.51) \times 10^{-2}$
[29]	11 GHz	2.84	$2 \times 10^{-2}$
Proposed method	63MHz	3.18	0.012
	128MHz	3.08	0.013
	300 MHz	3.11	0.014
MPR	Frequency	$\epsilon_r'$	$\tan\delta$
[30]	100 Hz	4.9	$2 \times 10^{-2}$
Proposed method	63MHz	4.11	0.025
	128MHz	4.12	0.023
	300 MHz	4.10	0.027